Mechanism of allosteric activation of human mRNA cap methyltransferase (RNMT) by RAM: insights from accelerated molecular dynamics simulations

Juan A. Bueren-Calabuig [ID][1,*], **Marcus G. Bage[1], Victoria H. Cowling[2] and Andrei V. Pisliakov[1,3,*]**

[1]Computational Biology, School of Life Sciences, University of Dundee, Dundee, DD1 5EH, UK, [2]Centre for Gene Regulation and Expression, School of Life Sciences, University of Dundee, Dundee, DD1 5EH, UK and [3]Physics, School of Science and Engineering, University of Dundee, Dundee, DD1 4HN, UK

ABSTRACT

The RNA guanine-*N7* methyltransferase (RNMT) in complex with RNMT-activating miniprotein (RAM) catalyses the formation of a N7-methylated guanosine cap structure on the 5′ end of nascent RNA polymerase II transcripts. The mRNA cap protects the primary transcript from exonucleases and recruits cap-binding complexes that mediate RNA processing, export and translation. By using microsecond standard and accelerated molecular dynamics simulations, we provide for the first time a detailed molecular mechanism of allosteric regulation of RNMT by RAM. We show that RAM selects the RNMT active site conformations that are optimal for binding of substrates (AdoMet and the cap), thus enhancing their affinity. Furthermore, our results strongly suggest the likely scenario in which the cap binding promotes the subsequent AdoMet binding, consistent with the previously suggested cooperative binding model. By employing the network community analyses, we revealed the underlying long-range allosteric networks and paths that are crucial for allosteric regulation by RAM. Our findings complement and explain previous experimental data on RNMT activity. Moreover, this study provides the most complete description of the cap and AdoMet binding poses and interactions within the enzyme's active site. This information is critical for the drug discovery efforts that consider RNMT as a promising anti-cancer target.

INTRODUCTION

Enzymatic modification of the 5′-end of eukaryotic messenger RNA by the addition of a cap structure is a key process that provides protection against 5′-exonucleases and facilitates the export and translation of mRNA (1–4). The cap is formed on the first transcribed nucleotide of the pre-mRNA as a result of three consecutive enzymatic reactions: (i) the 5′ end triphosphate of pre-mRNA is hydrolysed to diphosphate by a 5′-triphosphatase; (ii) GMP is added by the RNA guanylyltransferase to create the cap intermediate GpppN, with a 5′→5′ triphosphate linkage and (iii) the RNA guanine-*N7* methyltransferase (RNMT) catalyses the transfer of a methyl group from S-adenosylmethionine (AdoMet) to GpppN to create the mature cap, m7GpppN, and byproduct, AdoHcy (S-adenosyl homocysteine) (Figure 1A) (2). This capping mechanism targets the nascent RNA polymerase II transcripts (i.e. pre-mRNAs) and is conserved amongst eukaryotes and viruses, although structural organization of enzymes varies between organisms, e.g. the capping process can be carried out by a single complex or multiple enzymes (2,5).

In vertebrates, RNMT is activated by the RNMT-activating mini-protein (RAM) that has been shown to be required for efficient cap methylation, mRNA translation and cell viability (6,7). RNMT has basal activity that increases 5- to 10-fold in the presence of RAM (8). Grasso *et al.* demonstrated that regulation of RNMT–RAM complex has a crucial role in the gene expression changes needed during cell differentiation and reprogramming. In particular, the RNMT–RAM complex is important for pluripotency-associated gene expression. RAM is highly expressed in embryonic stem cells; during neural differentiation, RAM is repressed while high RNMT levels are maintained contributing to down regulation of pluripotency-
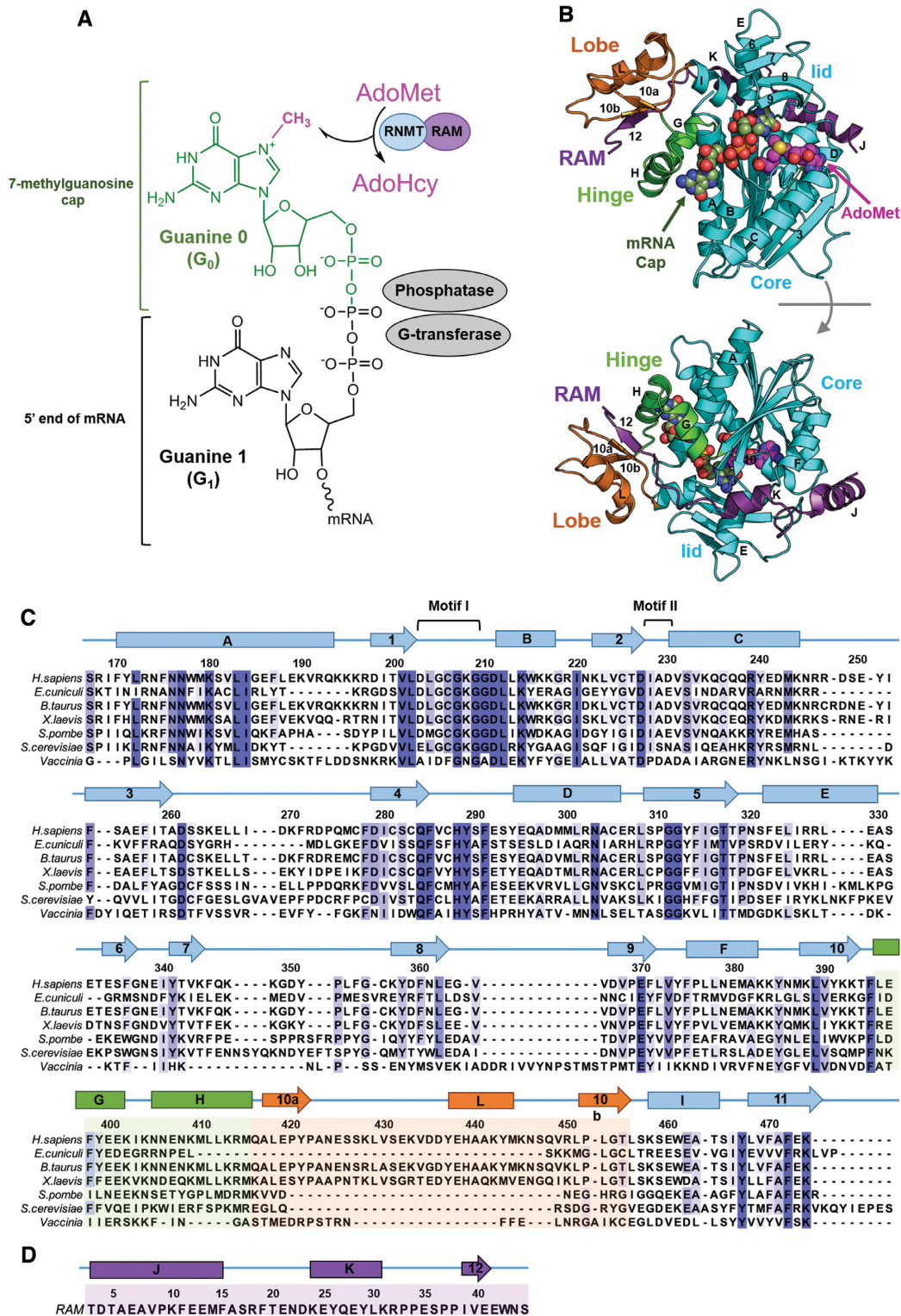
Figure 1. mRNA cap and mRNA methyltransferases. (**A**) Structure of mRNA cap and mRNA capping enzymes. The G_0, G_1 and methyl (CH_3) groups of the cap are labelled. Three enzymes involved in a stepwise formation of the cap, namely G-transferase, phosphatase and methyltransferase (RNMT), are indicated next to the respective chemical group. RNMT catalyses transfer of a methyl group from AdoMet to G_0 at N7 position, producing a by-product AdoHcy. (**B**) Structure of the human RNMT–RAM complex (PDB ID: 5E8J). RNMT core (residues 165–476) is shown in cyan, the α-helix hinge (residues 395–415) in green and the modular lobe (residues 416–456) in orange. Nomenclature of key helices and strands is shown. RAM (residues 2–45) is displayed in violet. Representative binding poses of AdoMet and cap (G_0pppG_1) are shown using the spheres representation (also see Figure 3). (**C**) Multiple sequence alignment of human RNMT with its orthologs from a selection of eukaryotic organisms and viruses. The nomenclature of structural features shown was kept in line with Fabrega *et al.* (13) and Varshney *et al.* (8). The elements of the RNMT core are shown in cyan, α-helix hinge in green, and modular lobe—in orange, consistent with (**B**). (**D**) Sequence and secondary structure elements of RAM (residues 2–45).

associated genes and the emergence of the neural phenotype (9).

Recently, we reported the crystal structure of the catalytic domain (residues 165–476) of human RNMT in complex with the RNMT activation domain of RAM (residues 2–45) and AdoHcy (PDB ID: 5E8J) (8). Human RNMT consists of a catalytic domain (residues 121–476), homologous to other eukaryotic cap methyltransferases, and an N-terminal regulatory domain (residues 1–120) that facilitates the recruitment to RNA polymerase II transcription initiation sites (10,11) and regulates RNMT activity (12). The presence of RAM permitted the stabilization and crystallization of RNMT together with its modular lobe (residues 416–456), which was unresolved in previously reported structures of isolated RNMT (PDB IDs: 3BGV, 5E9W). This strongly suggested that the lobe is disordered in the absence of RAM.

The human RNMT has notable structural similarity to *Encephalitozoon cuniculi* mRNA cap methyltransferase Ecm1 despite having <40% sequence identity (13); the only major structural difference is the absence of the modular lobe in Ecm1. The core of the catalytic domain of RNMT displays the canonical Class I methyltransferase fold with alternating β strands (β1-β7) and α helices (αA- αE) (Figure 1B and C) (14). The lobe and an α-helix hinge containing helices αG and αH (residues 395–415) constitute a positively charged groove that accommodates the RNMT-activating domain of RAM (residues 1–45) (8). In particular, the extended RAM region (residues 32–42) establishes several polar and hydrophobic interactions within the lobe and the α-helix hinge, while the more ordered N-terminal end of RAM (residues 1–31) interacts with helices αE, αD and β7- β8 loop.

Our recent findings showed that RAM was key to enhance the methyltransferase activity of RNMT despite its distal location to the active site of the enzyme (7,8,15). The results obtained from crystal structures, biochemical assays and molecular dynamics (MD) simulations suggested that RAM is critical for maintaining the stability and structure of the RNMT lobe. This stabilization promotes the binding of AdoMet and induces a significant increase in the methyltransferase activity in the presence of RAM as a result of a series of interactions affecting the α-helix hinge, α-helix A and multiple active site residues (8). However, details of the allosteric mechanism by which RAM activates RNMT and promotes recruitment of RNMT substrates—AdoMet cofactor and cap substrate—remain elusive. Moreover, the available crystal structures of RNMT do not provide a clear insight into the binding mode of the substrates: the human RNMT–RAM complex and *Vaccinia* virus mRNA methyltransferase were solved only in the presence of the byproduct AdoHcy (8,16). A set of crystal structures was reported for Ecm1 that included the methyltransferase in complex with individually bound ligands (AdoMet, AdoHcy and the cap analogue); however, the optimal poses of two substrates simultaneously bound could not be clearly revealed (13). Despite the concerted efforts of X-ray crystallography, biochemistry and computational biophysics in the attempt to understand RNMT activity and regulation, the binding modes of the RNMT substrates as well as the allosteric mechanism of RNMT activation by RAM remain

unresolved issues. Therefore, an alternative approach needs to be taken in order to elucidate these key aspects of RNMT functioning. In this work, we shed light on these questions through a comprehensive computational study, employing a combination of several molecular simulation methods.

Over the past decade, MD simulations have become increasingly important in solving the atomic-level mechanisms of protein allostery, often revealing missing features that purely experimental techniques could not provide (17–20). However, a lack of sufficient sampling of events that take place on very large timescales constitutes a significant limitation when employing standard MD simulations to explore allosteric mechanisms. In order to overcome this problem, enhanced sampling simulations have shown to be extremely valuable for more efficient sampling of the conformational space of large biomolecular systems while using significantly less computational resources (21–26). In this study, we employ both standard (or conventional) molecular dynamics (cMD) and accelerated molecular dynamics (aMD) to: (i) elucidate the binding mode of RNMT substrates, cap and AdoMet, bound simultaneously to the enzyme's active site and (ii) explain the allosteric mechanism by which RAM efficiently stimulates RNMT activity. Extensive simulations offer a detailed picture of the conformational changes occurring at the active site of the enzyme that promote binding of the reaction substrates and modulate the activity of RNMT. Furthermore, by performing community network analysis we provide evidence of the allosteric paths that connect RAM to the RNMT active site, thus offering the first comprehensive description of the molecular mechanisms of RNMT activation by RAM.

MATERIALS AND METHODS

Systems setup

The crystal structure of the human RNMT in complex with RAM and with the bound AdoHcy was recently reported by our group (8). The suite of crystal structures previously reported by Fabrega *et al.* (13) elucidated the binding poses of AdoMet, AdoHcy and cap to *E. cuniculi* Ecm1 methyltransferase. However, the simultaneous binding mode of both substrates remained elusive in either of the structures. Using these structures, we constructed a set of simulation systems to selectively investigate (i) the binding modes of the substrates in the RNMT active site and (ii) the allosteric activation of RNMT by RAM. A summary of systems and all molecular dynamics simulations performed in this work is provided in Table 1, and the details of the protocol are given below.

apo-RNMT +/−RAM. The crystal structure of human RNMT (residues 165–476) in complex with the full-length RAM (residues 2–45) (PDB ID: 5E8J) (8) was used for simulations of RNMT with and without RAM; in the latter case RAM was removed.

apo-RNMT +RAM (20-45). The role of the N-terminal region of RAM in the activation of RNMT was investigated by simulating RNMT in complex with a *truncated* form of RAM (residues 20 to 45), in which the N-terminal part of RAM (residues 2–19) was removed.

Table 1. Summary of molecular dynamics simulations performed in this work

	System	cMD	aMD
1	apo RNMT	100 ns	200 ns
2	apo RNMT-RAM	100 ns	200 ns
3	apo RNMT-RAM (res 20–45)	100 ns	200 ns
4	RNMT-RAM · Cap + AdoMet	100 ns	200 ns
5	RNMT-RAM · Cap	100 ns	200 ns
6	RNMT · Cap + AdoMet	100 ns	200 ns
	Total simulation time:	600 ns	1.2 μs

RNMT–RAM complex with substrate(s). The substrates—AdoMet and the cap analogue G_0pppG_1 ('cap' throughout this paper) (Figure 1A)—were modelled simultaneously into the RNMT–RAM complex: (i) the bound AdoHcy in the crystal structure of human RNMT–RAM (PDB ID: 5E8J) (8) was modified to AdoMet; (ii) the position of the cap analogue was obtained by superimposing the resulting structure with the *E. cuniculi* Ecm1 structure, which was solved with the cap (PDB ID: 1RI2) (13). Within the cap analogue, 'G_0' corresponds to the guanine to be methylated by RNMT and 'G_1' corresponds to the first nucleotide within the pre-RNA transcript (see Figure 1A). One of the simulated systems (system 5 in Table 1) contained only the cap bound to RNMT–RAM, but not AdoMet.

All models were prepared with the LEaP utility from the AMBER14 suite of programs (27) using the ff14SB force field (28). To neutralize the terminal groups the N-terminus of RNMT was capped with an acetyl group (ACE), and the N- and C-termini of RAM were capped with ACE and a methylated amino group (NME), respectively.

The geometries of the ligands were refined with Gaussian03 (29) at the HF/6-31G* level. The optimized geometries were used to calculate the electrostatic potential-derived (ESP) charges using the RESP methodology (30), as implemented in the *antechamber* module in Amber14 (27). The force field parameters for AdoMet were generated with *antechamber* module, using the general AMBER force field (GAFF) (31).

Each simulation system was immersed in a cubic box of TIP3P water molecules that extended at least 15 Å away from the protein, and then was neutralized by adding the appropriate number of counterions (32). This was followed by steepest-descent energy minimization to remove steric clashes.

Molecular dynamics simulation protocols

All MD simulations were performed using the pmemd.cuda module of AMBER14. Periodic boundary conditions were used. The cut-off distance for the non-bonded interactions was 10 Å. Electrostatic interactions were treated using the smooth particle mesh Ewald method (33). The SHAKE algorithm was applied to all bonds involving hydrogens, and an integration step of 2.0 fs was used throughout (34). Each system was heated to 300 K over a 50 ps interval using a weak coupling algorithm (35). A 200 ps equilibration was performed to allow the solvent to redistribute around the positionally restrained protein. The system was subse-

quently allowed to evolve unrestrained at constant temperature (300 K) and pressure (1 atm) using the weak-coupling algorithm (35). Atomic coordinates were saved every 20 ps for further analysis. Each system was initially simulated using conventional molecular dynamics (cMD) for 100 ns.

Accelerated molecular dynamics (aMD)

The activation mechanism of RNMT involves protein–protein binding, domain conformational changes and long-distance correlated motions that often occur over very long timescales that are difficult to reach by cMD. To overcome this limitation, accelerated molecular dynamics introduces a positive boost energy to the potential energy function, effectively reducing the height of energetic barriers and enhancing conformational sampling (36–38). Contrary to other enhanced sampling protocols such as metadynamics (39,40), aMD does not require predefined collective variables to initiate the enhanced sampling and has been successfully applied in several biomolecular systems to significantly improve the sampling of long-time scale event including allosteric mechanisms (41–44).

In aMD, a boost potential, $\Delta V(r)$, is applied when the average potential energy of the system, $V(r)$, is below a previously defined reference potential energy E_P. The modified potential, $V^*(r)$, used for MD simulations, is then given by Equation 1:

$$\begin{cases} V^*(r) = V(r), & \text{if } V(r) > E_P \\ V^*(r) = V(r) + \Delta V(r), & \text{if } V(r) < E_P \end{cases} \quad (1)$$

In this work, 200 ns aMD simulations were performed for each system (Table 1), using a 'dual-boost' protocol. This included a boost potential energy applied to all the atoms in the system and an extra dihedral boost applied to the torsion angles:

$$V(r) = \frac{(E_P - V(r))^2}{\alpha_P + E_P - V(r)} + \frac{(E_D - V_D(r))^2}{\alpha_D + E_D - V_D(r)} \quad (2)$$

where V_D is the dihedral energy, E_P and E_D are the reference potential and dihedral energies, and α_P and α_D are the acceleration parameters that describe the strength of the boost for each term and determine the shape of the modified potentials. The parameters of the aMD simulation (E_P, α_P, E_D, α_D) were initially selected following the guidelines from previous works (44–46) and then further adjusted after preliminary aMD simulations (Supplementary Table S1).

Analysis of MD trajectories

Protein structures and MD trajectories were visually inspected using the molecular visualization programs Py-MOL (47) and VMD (48). Interatomic distances and angles, root-mean-square deviations and fluctuations (RMSD and RMSF) with respect to a reference structure and secondary structure analysis were monitored using the CPP-TRAJ module in AmberTools 15 (27). Residue-per-residue cross-correlations analysis of the RNMT–RAM complex was performed using CPPTRAJ (27,49) using the backbone Cα fluctuations. The 2D schemes of the ligand–protein interactions were obtained using Ligplot+ (50). MDpocket

(51) was used to evaluate the AdoMet and cap (G_0) pocket volumes during the aMD simulation of each system. The two ligand pockets were defined in the reference system (RNMT–RAM with the bound cap and AdoMet) with MDpocket using 2000 snapshots from the aMD trajectory. The resulting grids were then superimposed on each simulated system and the volumes of the two ligands pockets were monitored along the 200 ns aMD trajectories. MDpocket was run using 10 000 Monte Carlo iterations for each system. The minimum and maximum radii of the probe ('alpha') spheres in each pocket were 3 and 6 Å, respectively. Electrostatic potentials were calculated using the Adaptive Poisson-Boltzmann Solver (APBS) with PyMol APBS tools (52).

Free energy landscapes (FELs)

Free energy landscapes (FELs) were constructed for each system to characterize the 'open' / 'closed' RNMT active site conformations sampled during the aMD simulations. Two collective variables (CVs) that could discriminate between several active site conformations were identified: CV1 describes the accessibility to the cap binding pocket and was defined as the centre of mass (COM) distance between the upper half of RNMT α-helix A (residues 2–11) and the β8–β9 loop (residues 362–366); CV2 describes the accessibility to the AdoMet-binding pocket and was defined as the COM distance between Motif I (residues 205–209) and the β4-αD loop (residues 285–289), as shown in Figure 5A. The cap guanine pocket was considered to be accessible ('cap-open' state) when CV1 is >10 Å, which favoured binding of G_0 to the cavity created between α-helix A and the β lid. The AdoMet-binding pocket was considered to be open and accessible to AdoMet when CV2 was >11 Å. The 'fully open' conformation of RNMT is only obtained when CV1 and CV2 are greater than 10 and 11 Å respectively, allowing the access of both substrates. A 'closed' conformation is obtained when CV1 and CV2 are below 9 and 10 Å, respectively.

Convergence of conformational FELs was tested by using different amounts of sampling in aMD simulations. The overall shape of FELs as well as positions and relative populations of minima were maintained for different amounts of sampling. Convergence was additionally tested using four different bin sizes for CVs. The FELs presented in this paper were constructed using a bin size of 0.3 Å for both CVs.

In principle, aMD simulations can recover the equilibrium properties of the unbiased potential by reweighting statistics using the Boltzmann factor of the boost potential $e^{\beta \Delta V(r)}$ (38). However, in aMD simulations of large biomolecular systems with highly complex energy landscapes, large values of boost potentials are normally used to gain sufficient sampling, which leads to high 'energetic noise' during the reweighting process (53,54). Hence, only unweighted FELs are presented in this work. These unweighted FELs were calculated for each simulated system and are used for comparison purposes only, providing an estimate of the free energy differences; this procedure is in line with previous aMD studies of large biomolecular systems (42,55,56).

Community network analysis

Allosteric networks in the RNMT–RAM complex were studied by means of community network analysis using the NetworkView plugin in VMD (57,58). The protein system in the molecular dynamics simulations is represented as a set of 'nodes' corresponding to each protein residue. Edges connecting pairs of nodes are drawn when two residues are within 4.5 Å of each other for at least 75% of the aMD trajectory, yielding a complex all-residue network. To obtain a simplified and easier to interpret coarse-grained representation, the resulting network map is decomposed into 'communities' using the Girvan–Newman algorithm (59): large groups of strongly connected nodes (i.e. residues) are clustered into communities, which are then loosely connected to one another by edges. The edges are weighted to reflect strength (so-called cumulative betweenness) of the interactions between communities and thus help to identify potential connectivity pathways (60). The community networks are represented in diagrams displaying the communities as circles, with radii proportional to the number of residues comprising a community, connected by edges, whose widths are proportional to the strength of the intercommunity interaction.

RESULTS

Binding modes of AdoMet and cap to RNMT

Our first goal was to elucidate the reactive configuration of substrates in the active site of RNMT. Since the crystal structure of human RNMT (or homologous mRNA methyltransferases) in complex with two simultaneously bound substrates is not available, we have built the RNMT–RAM system in complex with AdoMet and cap (see details in 'Materials and Methods' section). The obtained model was then simulated using both cMD and aMD methods. The complex was first relaxed for 100 ns using unrestrained cMD (Figure 2A). In order to sample more efficiently the protein free energy landscape and possible allosteric effects, which often take place on long timescales, the relaxed system was simulated for 200 ns using aMD.

RNMT–RAM structure and conformational dynamics in the presence of ligands. aMD simulations of the RNMT–RAM complex in the presence of AdoMet and cap showed a high degree of stability of the key RNMT structural elements (Figure 2B). The core domain of RNMT (residues 165–394) as well as the α-helix hinge element (residues 395–415) remain stable throughout the trajectory (average RMSD 1.5 Å) and maintain structural features observed in the crystal structure of human RNMT–RAM (8). In particular, the α-helix A (residues 170–194), which is positioned adjacent to the cap binding site, keeps its original conformation (RMSF 0.8 Å), in which it interacts with the α-helix hinge (Figure 2A and C). Strands β8 and β9 (residues 356–362, 365–371), which form a 'lid' for the cap binding pocket similar to the one observed in the Ecm1 methyltransferase (13), also remain highly stable during the trajectory (RMSF 1.3 Å). The region displaying the highest degree of flexibility was the lobe (residues 416–456). That was mainly due to a long loop connecting strand β10a and α-helix L.
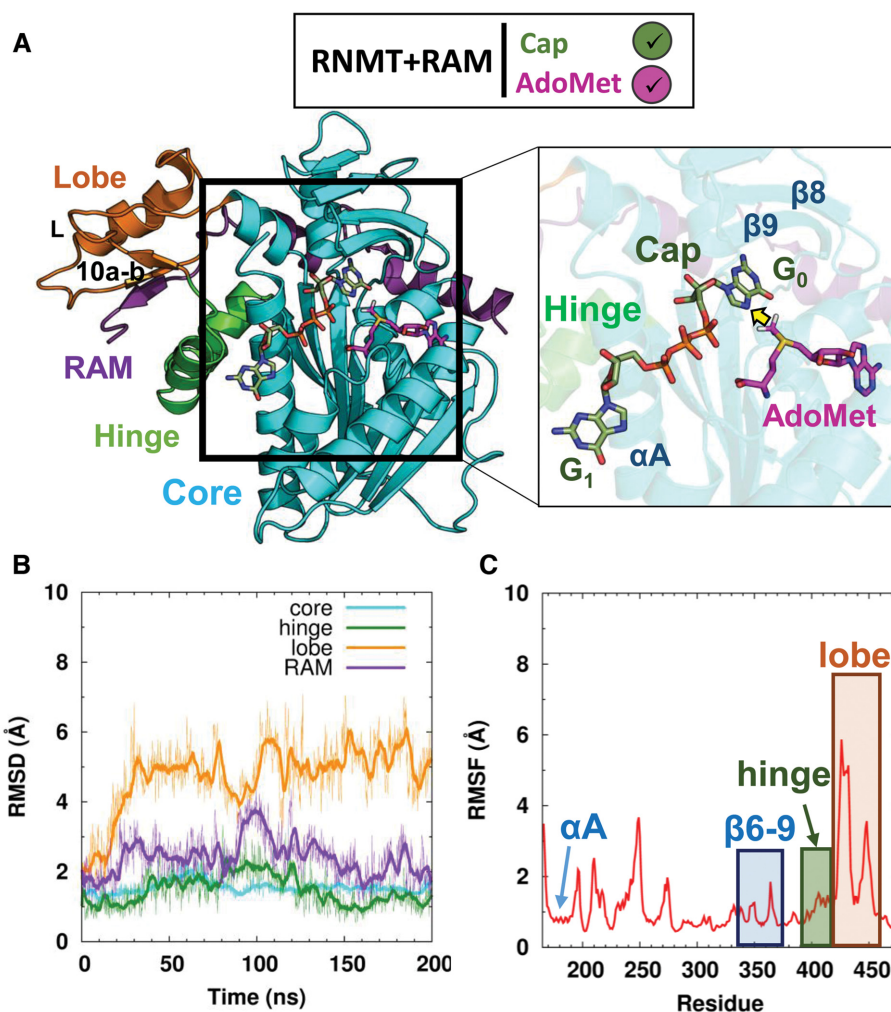
Figure 2. Characterization of the RNMT–RAM complex in a simulation with bound AdoMet and cap. (**A**) Structural model of RNMT–RAM (cartoon representation) in complex with AdoMet and cap (stick representations, with magenta and green carbon atoms, respectively). A close-up view shows the ligands within RNMT in a methyl-transfer reactive conformation; the transferred methyl group is indicated by a yellow arrow. Relevant structural elements of RNMT are labelled. In all figures, the simulation systems are schematically annotated by the legend boxes, which specify the presence/absence of RAM (+RAM or RAM omitted) and substrate(s) (ticked green/magenta or empty grey circles for Cap/AdoMet). (**B**) Time evolution of backbone RMSD (in Å) of the key structural elements of RNMT during the aMD simulations. (**C**) RMSF values (in Å) of the RNMT residues obtained from aMD simulations.

Nonetheless, the secondary structure elements were maintained along the aMD trajectory in all regions of RNMT, including the lobe. The ordering of the lobe was a result of multiple polar interactions with the activation domain of RAM (residues 2–45), which binds to a positively charged surface groove, as detailed in our previous work (8). Thus, RAM introduces a high degree of stability of the catalytic domain of RNMT. Overall, the protein structure and conformational dynamics observed in the aMD simulation in the presence of AdoMet and cap were very similar to that of *apo*-RNMT–RAM in the crystal structure and our previous cMD study (8). This gives support to the obtained structural model, which describes the simultaneously bound reaction substrates (AdoMet and cap), their binding poses and interactions within the RNMT active site—an important information missing in the crystallographic structures available to date.

AdoMet binding mode. AdoMet binds into a pocket formed by strands β1 and β2, adopting a conformation common to AdoMet-dependent methyltransferase enzymes (8,13,14,16). No significant differences were observed between the AdoMet conformation obtained in this study (Figure 3A; see also Supplementary Table S2) and the Ado-Hcy binding pose in the RNMT crystal structure (8). The carboxylate group establishes a salt bridge interaction with K180, a known key residue for RNMT activity (8), which is located within the α-helix A. The amino acid moiety of AdoMet also interacts with the glycine-rich loop that connects strand β1 and α-helix B and includes the conserved 'Motif I' (Glu/Asp-X-Gly-X-Gly-X-Gly; residues 203–210) (Figure 1C). The amino group of AdoMet forms a hydrogen bond with the carbonyl oxygen of G205. In addition, the 2′ and 3′-hydroxyls of the adenosine ribose interact with D227 within the 'Motif II' loop (residues 227–230), and non-polar contacts are established with I228. The long loop connect-
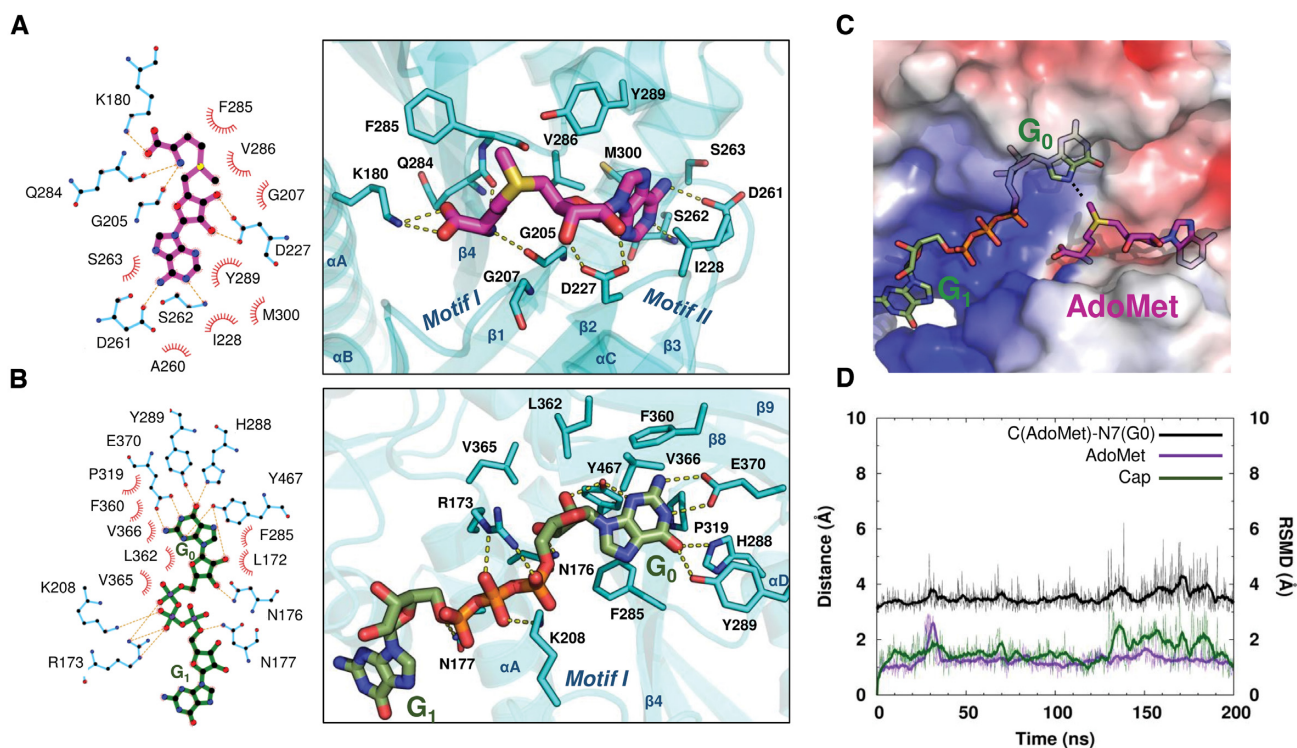
Figure 3. Binding modes of AdoMet and cap in the RNMT active site. (**A**) 2D protein–ligand interaction map of RNMT and AdoMet (magenta) (left), and a representative aMD snapshot of AdoMet bound to the RNMT active site (right). (**B**) 2D protein–ligand interaction map of RNMT and cap (green) (left), and a representative aMD snapshot of cap bound to the RNMT active site (right). (**C**) Electrostatic potential surface representation of the RNMT active site, AdoMet and cap binding pockets. Electrostatic potentials are coloured from the most negative (red, $-5\ k_{\mathrm{B}}T/e$) to neutral (white, $0\ k_{\mathrm{B}}T/e$) to the most positive (blue, $+5\ k_{\mathrm{B}}T/e$). (**D**) Time-evolution of the distances between AdoMet (carbon atom of the methyl group) and the cap G_0 (N7 atom) (black line) in the aMD simulation; the monitored distance between the groups is indicated by a white dotted line in panel (C). The RMSDs of AdoMet (magenta) and cap (green) are plotted against the secondary (right) vertical axis.

ing strands β3 and β4 has an important role in stabilizing AdoMet by establishing two hydrogen bonds between the adenine atoms N6 and the side chain of D261 as well as between the adenine N1 and the backbone N of S262. Q284 in strand β4, establishes a hydrogen bond with the amino group of AdoMet whereas V286 within the β4-helix αD loop stabilizes the adenine base through hydrophobic interactions with V286. As a result, AdoMet is stabilized within a pocket displaying a negative electrostatic potential due the presence of D227 and the carbonyl oxygens of Q284 and F285, which is also favourable for the stability of the AdoMet sulfonium ion (Figure 3C). It is important to note that the above-mentioned residues involved in binding of AdoMet are highly conserved (Figure 1C), highlighting that the catalytic domain of RNMT has high sequence similarity and shares structural and functional features with similar mRNA methyltransferases.

Cap binding mode. G_0 of the cap binds within a pocket located between the β4 strand-α-helix D loop, which constitutes the 'floor' of the pocket, and strands β8–9 that form a lid over the cap binding site (Figure 3B), in a similar fashion to what was suggested for Ecm1 (13). The active site residues establish a number of non-polar and hydrogen-bonding and salt-bridge interactions with the cap groups (Supplementary Table S2). F285 establishes a stacking interaction with G_0. On the right-hand side of the active site

(Figure 3B), H288 (Nε) and Y289 (OH) form two hydrogen bonds with the guanine O6. P319 contributes to guanine stabilization by establishing hydrophobic interactions with the cap. Key hydrophobic interactions are observed between G_0 and β-lid residues F360, L362, V365 and V366. The end of the lid is formed by E370 that establishes two hydrogen-bond interactions with the G_0 N1 and N2. Importantly, Y467 located at the back of the pocket establishes two hydrogen bonds with N3 and O2′. The left-hand side of the pocket (Figure 3B) is formed by key residues located on the α-helix A: R173 forms several polar interactions with the triphosphate chain connecting G_0 with G_1, whereas Nδ's of N176 and N177 form hydrogen bonds with the ribose O3′ and the cap phosphate groups, respectively. Interestingly, K208, located in the key loop responsible for AdoMet binding ('Motif I'), establishes two salt bridges with α and β phosphates of the mRNA cap, thereby providing a conduit between the AdoMet- and cap-binding sites, and a potential structural linkage for allosteric communication between these sites. Finally, the electrostatic surface representation of the cap binding pocket revealed an extended, highly positive region fitting the polyphosphate chain of the cap, with contributions from R173, K180, K208, R239 and R246 (Figure 3C). The G_0 pocket displays a more neutral surface that is favourable for substrate binding. Similar to the AdoMet pocket, the residues involved in binding of

the G_0 and polyphosphate chain of the Cap are highly conserved (Figure 1C).

The above-detailed multiple RNMT–ligand interactions enabled tight binding of AdoMet and cap in the presence of RAM, as demonstrated by a very high degree of stabilization of both ligands during long unrestrained cMD and aMD simulations: the average RMSD values were about 1.5 Å for both ligands (Figure 3D); ligand dissociation or at least substantial deviations from the original structure were not observed. In addition, the ligands maintain the conformation optimal for the AdoMet-to-cap methyl transfer (Figure 3D): the distance between the AdoMet CH_3 and the methyl acceptor (G_0 N7) was maintained at around 3.7 Å (a structure of the representative snapshot is included in Supplementary Data in the PDB format). During the cMD and aMD simulations, no direct contacts were observed between RNMT and the N7 atom of G_0, the sulphur atom of AdoMet or the methyl group of AdoMet, in line with the models suggested by Fabrega *et al.* (13).

In order to explore possible origins of the cooperativity between RAM on the substrates binding, an additional system, namely RNMT with the bound AdoMet and cap but in the absence of RAM, was simulated using the same protocol; the results are shown in Supplementary Figure S1. In terms of ligand interactions and dynamics, this system displayed very similar behaviour to that in the presence of RAM (Figure 3D), showing identical ligand binding poses and interactions with the active site residues, as well as similar RMSD values for both ligands; the methyl-transfer distance was also maintained. This illustrates that RAM does not affect stability of ligands in the active site once they are bound there. It should be mentioned that this does not rule out a direct role of RAM in the subsequent catalytic mechanism, e.g. through electrostatic interactions (61). In the RNMT structure, as expected, the only major change was the disordering of the modular lobe region that occurs in the absence of RAM, whereas α-helix A, the α-helix hinge and strands β6–9 maintained the same overall conformations.

In summary, cMD and aMD simulations offered a detailed picture of the AdoMet and cap binding poses and interactions within the RNMT active site, which complements and is consistent with previous structural and biochemical data. This provides the most complete description of the binding modes of the substrates within the RNMT active site to date. Nonetheless, and despite the stabilization effect observed by RAM on the overall RNMT structure and dynamics, the mechanism by which RAM regulates RNMT activity remained unclear. Hence, we next investigated whether RAM can allosterically regulate RNMT activity through selection of specific RNMT conformations that could enhance binding of AdoMet and cap to the active site.

RAM stabilizes RNMT and enhances the active site conformations promoting the substrates binding

As our simulations revealed no effect of RAM on the poses and interactions of two substrates when bound in the RNMT active site, next we explored an alternative explanation of the RNMT activity modulation by RAM: we investigated whether the role of RAM is to prepare the AdoMet and cap pockets for optimal binding of the ligands. We carried out cMD and aMD simulations of *apo*-RNMT in the presence and absence of RAM, focussing on the conformational changes in the previously characterized AdoMet and cap binding pockets. Furthermore, recent experimental data suggested that the cap binding could promote the binding of AdoMet to the RNMT–RAM complex following a cooperative binding model (8). To provide a molecular rationale for this observation, RNMT–RAM was also simulated in the presence of the cap only.

RAM modulates overall stability of RNMT. Analysis of *apo*-RNMT dynamics provided valuable insights into the allosteric effects induced by RAM (Figure 4). The RMSFs and RMSDs were computed from the aMD simulations of RNMT in the presence or absence of RAM. Consistent with the crystal structure and our previous cMD simulations of RNMT–RAM (8), the lobe region displays the highest flexibility in either system, though it is significantly higher in the absence of RAM (average RMSD of the lobe backbone atoms were 4.5 Å versus 8.0 Å with and without RAM, respectively) (Figures 4A and B). The calculated backbone RMSF values also highlight the stability brought about by RAM within the lobe region (Figure 4C). This disorder-to-order transition is achieved as a result of multiple RNMT–RAM interactions that enabled the crystallization of the modular lobe of RNMT only in the presence of RAM (8). The degree of flexibility of the lobe is directly correlated with that of the α-helix hinge, which remained remarkably stable in the RNMT–RAM simulation (Figure 4C). Conversely, disordering of the lobe observed in a simulation in the absence of RAM notably increased flexibility of the hinge and the upper half of α-helix A, which contains the important active site residues N176 and K180 (Figure 4D). Flexibility of strands β6-β9, which form the active site 'lid', was also significantly pronounced in the absence of RAM. Secondary structure analysis showed a progressive loss of strand elements in the β6-β9 region during the aMD simulation of RNMT, while they were maintained in the simulation of the RNMT–RAM complex (compare Figure 4E and F). Large flexibility of β8-β9 loop also correlated with disordering of strand β9, located in the upper region of the cap binding pocket and containing the residues V365, V366 and E370, which are important for binding of cap.

RAM selects the RNMT active site conformations optimal for substrates binding. Next, we investigated whether the observed RAM-modulated stabilization of various structural elements in *apo*-RNMT is also linked to changes in the active site, e.g. through promotion of certain conformations that favour binding of substrates. In order to quantify such effects, we introduced two descriptors of the substrate binding pockets, namely collective variables (CVs) 1 and 2 (Figure 5A). The two CVs were used to build unweighted free energy landscapes (FELs), which in a simple manner represent all the conformations of the active site of RNMT that were sampled during an aMD simulation and provide a straightforward characterization of the RNMT active site.

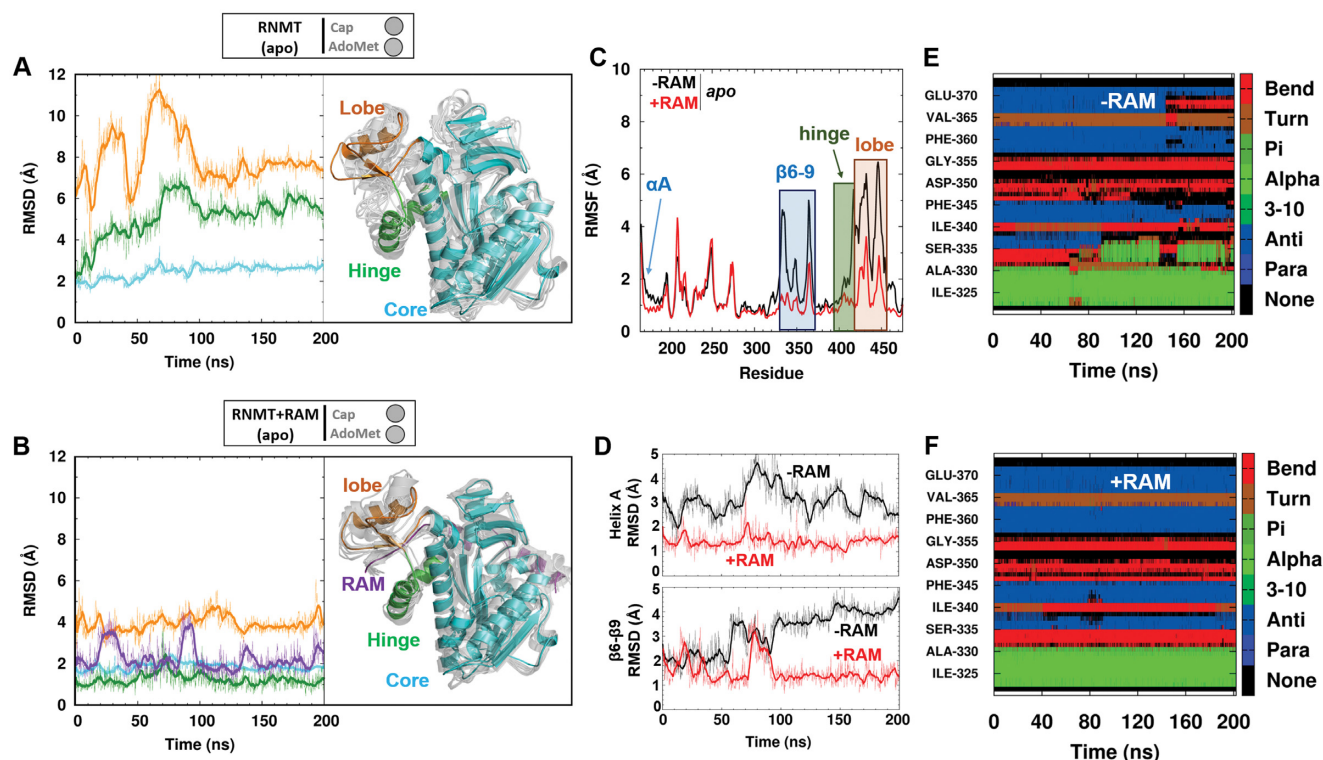As a reference we used the structural model of RNMT–RAM with the bound AdoMet and cap ligands, which nat-

Figure 4. Modulation of RNMT stability by RAM. (**A** and **B**) Left: Time evolution of the backbone atoms RMSD (in Å) of key structural elements of RNMT during the aMD simulation of *apo*-RNMT in the absence (A) and presence (B) of RAM. Right: A representative snapshot of *apo*-RNMT in the absence (A) and presence (B) of RAM displaying the key structural elements: catalytic core (cyan), hinge (green) and lobe (orange) regions. The representative snapshot is superimposed with multiple structures (light grey) that were sampled from the entire aMD trajectory and illustrate the range of conformational dynamics in each system. (**C**) The backbone RMSFs (in Å) of the catalytic domain of RNMT (residues 165–475) computed from the aMD simulation of *apo*-RNMT in the absence (black) and presence (red) of RAM. (**D**) Time evolution of the backbone RMSD (in Å) of α-helix A and strands β6–9 during the aMD simulation of *apo*-RNMT in the absence (black) and presence (red) of RAM. (**E** and **F**) Secondary structure analysis of the β-strand 'lid' region of RNMT (residues 320–375) performed on the aMD trajectories of *apo*-RNMT in the absence (E) and presence (F) of RAM.

urally provides the optimal conformations of each substrate pocket and of the entire active site ('fully open' conformation) (Figure 5B). The FEL obtained for this system shows a single free energy minimum, i.e. the conformation that was predominantly sampled during the simulation, which is located at CV1 = 11.5 Å; CV2 = 12.2 Å—a 'fully open' configuration favouring the binding of both substrates. In this conformation, the stability displayed by α-helix A and β8-β9 strands enables the correct docking of G_0. Motif I is stabilized by the K208-cap phosphate interaction, whereas Y289 interacts with G_0, E370 and the adenosine base of AdoMet. D227 in Motif II also interacts with the ribose hydroxyls of AdoMet. Overall, both AdoMet and cap binding pockets were strongly stabilized and sampled only in the 'fully open' conformation, as expected for the simulation in the presence of substrates.

The FEL of *apo*-RNMT in the absence of RAM displayed a global minimum located at CV1 = 7.8 Å, CV2 = 9.0 Å ('closed' conformation) (Figure 5C). In this conformation, the cap pocket is collapsed as a result of the displacement of α-helix A towards the guanine binding area and the partial loss of some secondary structure in the β lid (strands β8 and β9). The disordering and increased flexibility of strand β9 affects the position of the sidechain of Y289 that then flips towards the AdoMet binding site. In

addition, the sidechain of K208 reorients towards the electronegative AdoMet pocket and interacts with D227. As a result, the Motif I loop adopts an alternative conformation that obstructs AdoMet accessibility to the active site, thus leading to the 'closed' conformation. A second local minimum in this FEL is located at CV1 = 11.0 Å, CV2 = 8.5 Å, representing the 'cap-open' conformation (Figure 5C). This configuration would allow binding of cap as a result of a more favourable position of α-helix A and preserved structure of strands β8-β9. In contrast, accessibility for AdoMet to its pocket is limited: similar to the 'closed' conformation, Motif I loop is oriented towards the AdoMet binding site, blocking the access to AdoMet, despite the fact that Y289 is stabilized by E370. Altogether, this results in a conformation of the RNMT active site that offers binding of cap but not AdoMet, thus the 'cap-open' state. The population of this state is slightly lower than of the 'closed' state, and the barrier on the path between the two is low (~1.5 kcal/mol). Thus, the FEL illustrates a dynamic equilibrium between these two states as sampled in the aMD simulation. The 'fully open' conformation was poorly sampled in the aMD simulation of *apo*-RNMT (Figure 5C) suggesting that in the absence of RAM simultaneous binding of AdoMet and the cap is strongly disfavoured.
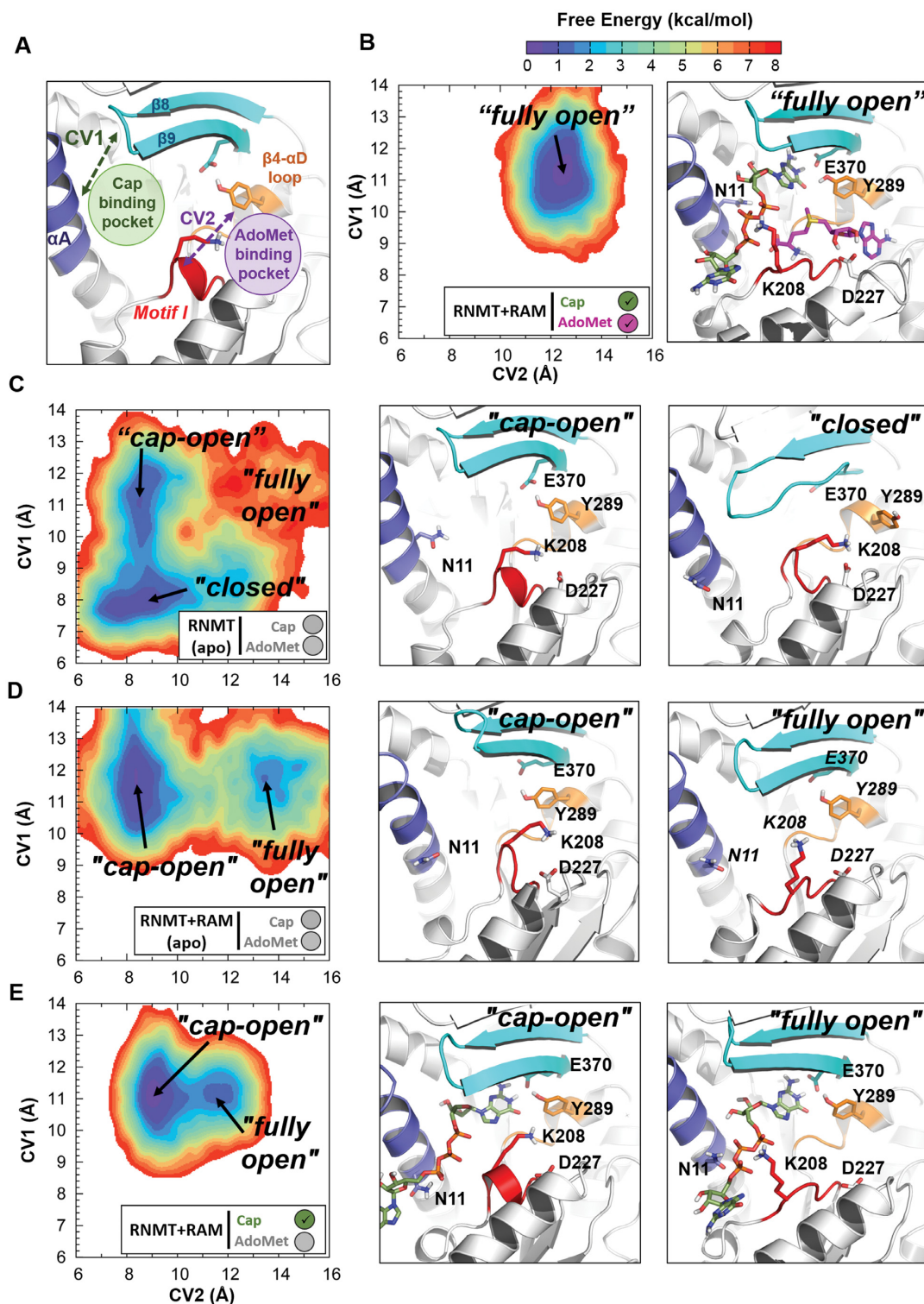
Figure 5. RAM-dependent modulation of the RNMT active site conformations. (**A**) Definition of collective variables (CVs) used to construct the free energy landscape (FEL) of RNMT. CV1 describes the cap binding pocket accessibility and is defined as the centre of mass (COM) distance between the upper half of the RNMT α-helix A (residues 2–11, highlighted in dark-blue) and the β8-β9 loop (residues 362–366, in cyan). CV2 describes the AdoMet binding pocket accessibility and is defined as the COM distance between Motif I (residues 205–209, in red) and the β4-αD loop (residues 285–289, in orange). (**B–E**) The conformational FELs of the active site of RNMT calculated for the simulation systems: (B) RNMT–RAM complex with the bound substrates AdoMet and cap; (C) apo-RNMT; (D) apo-RNMT in complex with RAM; and (E) RNMT-RAM complex with the bound cap. The FELs were built using all the snapshots from the corresponding aMD simulation and are shown as 2D contour plots with the lines in 0.5 kcal/mol increments. The colour scale corresponding to (unweighted) free energies is shown at the top. The simulation system is indicated by a legend in the box below the FEL. The most sampled conformational states, corresponding to the FEL minima, are labelled, and the corresponding representative structures of the RNMT active site are shown in the middle and right panels, next to the FELs.

The FEL obtained for the *apo*-RNMT in the presence of RAM showed a strikingly different picture (Figure 5D): in addition to the 'cap-open' state (located at CV1 = 11.9 Å, CV2 = 8.5 Å), which now represents a global minimum (i.e. the most populated conformation), the 'fully open' state (CV1 = 11.9 Å, CV2 = 13.5 Å) was now well sampled, while the 'closed' state completely disappeared. In the 'cap-open' conformation firmness of the cap pocket is facilitated by the Y289 interaction with E370, which stabilizes strand β9 of the β-lid. Similar to the *apo*-RNMT (no RAM) system, K208 is still flipped towards D227, inducing a conformational change in Motif I loop that limits accessibility to the AdoMet pocket in the 'cap-open' state. In contrast, in the 'fully open' state, the Motif I loop shifts towards the cap binding site, increasing the accessibility to the AdoMet pocket; the cap pocket still offers conformation suitable for the cap binding. The 'fully open' state displays a broader and more shallow landscape compared to the 'fully open' minimum in the presence of substrates (compare Figure 5D and B). This confirms that presence of the substrates stabilizes and significantly reduces the flexibility of the pockets. Moreover, the FEL showed a notable flattening of the region separating the 'cap-open' and 'fully open' conformations compared to the *apo*-RNMT system in the absence of RAM (Figure 5D versus 5C). This indicates that transitions from the 'cap-open' to the 'fully open' states are kinetically allowed in *apo*-RNMT–RAM.

In addition, the apo-RNMT–RAM system offered a clear illustration of the benefits of usage of enhanced sampling methodologies (here, aMD) to explore the RNMT active site conformations and free energy landscape (Supplementary Figure S2): while cMD simulation could only sample a single minimum, which corresponded to the starting conformation (i.e. the 'fully open' state), the use of aMD was key to unveiling a much greater region of the FEL, including the presence of the second, more stable minimum (the 'cap-open' state) as well as sampling the transition region between the two minima.

Our data reveal that in the presence of RAM, *apo*-RNMT will be predominantly found in a state suitable for cap binding (the 'cap-open' state), while in the absence of RAM the 'cap-open' state first needs to be reached from the 'closed' state. Importantly, the 'AdoMet-open' conformation, which would be with the AdoMet pocket open and the cap pocket closed, was never sampled in any of the studied systems. Altogether, our results show that RAM allosterically primes the RNMT active site for the cap binding. Furthermore, this strongly suggests the likely scenario in which the cap binding occurs first, and this promotes the subsequent AdoMet binding. This hypothesis is in agreement with our previous fluorescence polarization experiments that suggested that binding of the cap can enhance binding of AdoMet (8).

Additional support to this finding is provided by the results for the RNMT–RAM-cap system, which was simulated with the bound cap (but no AdoMet) using the same protocol (Figure 5E). As expected, the FEL showed a global energy minimum in the 'cap-open' state (CV1 = 11.0 Å, CV2 = 9.0 Å), which naturally favours the cap binding. The 'fullly open' conformation was also sampled although it can be seen (Figure 5E) that conformational space in this case was more restricted as a result of the extra stabiliza-

tion of the active site introduced by the presence of the cap. In this state K208 interacts with the polyphosphate chain of the cap, while the presence of the bound guanine (G_0) greatly stabilizes Y289. Both interactions ensure access to the AdoMet pocket, and thus the conformation favours the binding of AdoMet. Importantly, substantial flattening of the entire landscape as well as of the barrier between the 'cap-open' and 'fully open' states was observed and confirms the hypothesis that binding of the cap facilitates binding of AdoMet.

The distribution of the volume of the substrate pockets during the simulations was used as an additional quantitative measure to provide further details about the substrate binding mechanisms (Figure 6). This complements the free energy landscapes and conformational states reported in Figure 5. In *apo*-RNMT, the volumes of both the cap and AdoMet pockets are significantly reduced (thus collapsed, inaccessible pockets) when compared to those from the reference system (RNMT–RAM with the bound substrates) (Figure 6B). The presence of RAM significantly increases the volume of the cap pocket, whereas the AdoMet binding site remained largely inaccessible (Figure 6C). As expected, the binding of the cap ensured the optimal volume values of the G_0 pocket (Figure 6D). Interestingly, in the presence of the cap, the volume of the AdoMet binding pocket was still significantly lower than in the reference system. This is consistent with the fact that the preferred conformation in the cap-bound system was the 'cap-open' conformation and not the 'fully open' state (see Figure 5E). We can also interpret this as an indication of a plausible induced-fit binding mechanism for AdoMet, which is triggered by the K208 reorientation towards the cap polyphosphate chain.

Overall, analyses of the free energy landscapes and volumes of the binding pockets reveal that presence of RAM significantly enhances population of the 'cap-open' and 'fully open' conformations of RNMT, which are suitable for binding of substrates and particularly favourable for binding of the cap. This is consistent with the conformational selection mechanism of allostery. Furthermore, binding of the cap to the RNMT–RAM complex favours an active site conformation that is suitable for AdoMet binding, thus providing a rationale to the cooperative binding model suggested previously (8). In striking contrast, in the absence of RAM, RNMT displays significantly higher conformational flexibility and the 'closed' conformational state of the active site is predominantly sampled, in which binding of substrates is hindered.

An allosteric network mediates RNMT structural modulation by RAM

The results obtained from the aMD simulations suggest that RAM modulates the conformational changes in RNMT to alter its active site conformation. However, the precise mechanism of how this is achieved, i.e. specific interactions between RNMT and RAM and the way they are translated into conformational changes in the active site, remained unclear. In order to reveal the molecular origin of this regulatory effect and identify putative allosteric pathways, advanced post-processing analyses were performed on the aMD trajectories of the *apo*-RNMT–RAM complex;
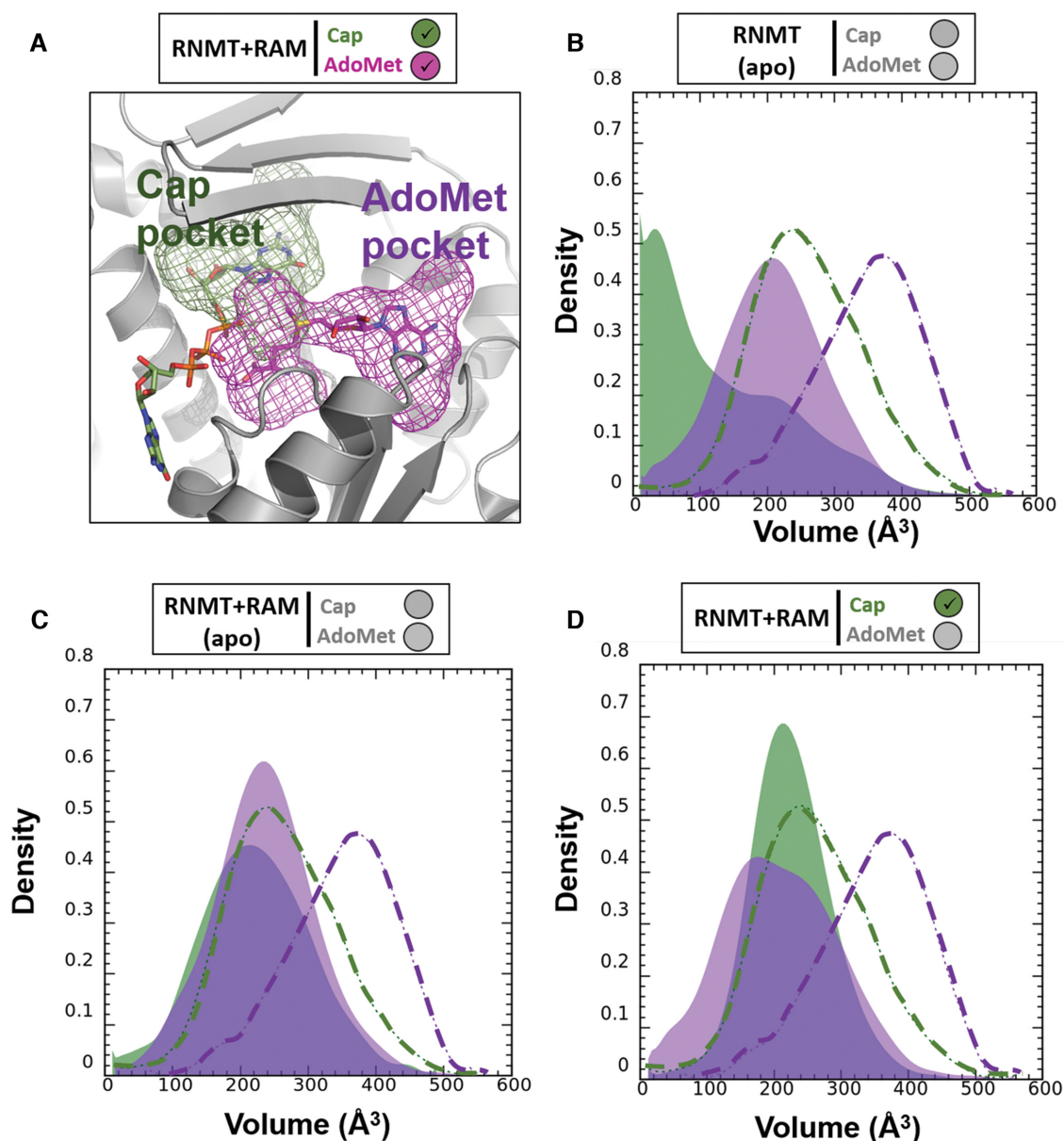
Figure 6. Distribution of the volume of the cap and AdoMet binding pockets. (**A**) The binding pockets of the cap (green) and AdoMet (magenta) were defined for the reference system (RNMT–RAM in the presence of both substrates) using MDpocket (see details in the 'Materials and Methods' section) and are shown as mesh surfaces. The ligands are shown as sticks inside the mesh surfaces. (**B–D**) Distribution of the volume of the cap (green) and AdoMet (magenta) binding pockets during the aMD simulations of: (B) *apo*-RNMT, (C) *apo*-RNMT in complex with RAM and (D) RNMT–RAM with the bound cap. The distributions obtained from the simulation of the reference system (RNMT–RAM with both substrates) are shown as dashed lines on each plot for comparison.

this included a residue-by-residue cross-correlation analysis, protein dynamic networks and a coarse-grained community network analysis (Figure 7).

Inter-residue correlation analysis of the *apo*-RNMT–RAM complex simulations revealed strong correlations between the key regions (Figure 7A). In particular, α-helix A was strongly correlated with the α-helix hinge and the lobe, and to a smaller extent with the β-strand lid. As expected, important correlated motions were also observed between the hinge and the lobe elements. Importantly, there is strong correlation between RAM and the structural elements forming the RNMT active site: in particular, the

N-terminal region of RAM (residues 2–20) correlates with strands β5, β6–7 and β8–9, whereas the C-terminal region of RAM (residues 30–45) correlates with the hinge, the lobe, α-helix I and, most notably α-helix A. Hence, a vast matrix of correlated dynamic motions connecting the RNMT key regions with the N- and C-termini of RAM provided additional evidence of the allosteric modulation fulfilled by RAM.

The all-residue dynamic network and coarse-grained community network analyses (58,62) were then performed to identify the allosteric paths for the RNMT regulation by RAM (Figure 7B). Both RNMT and RAM were included
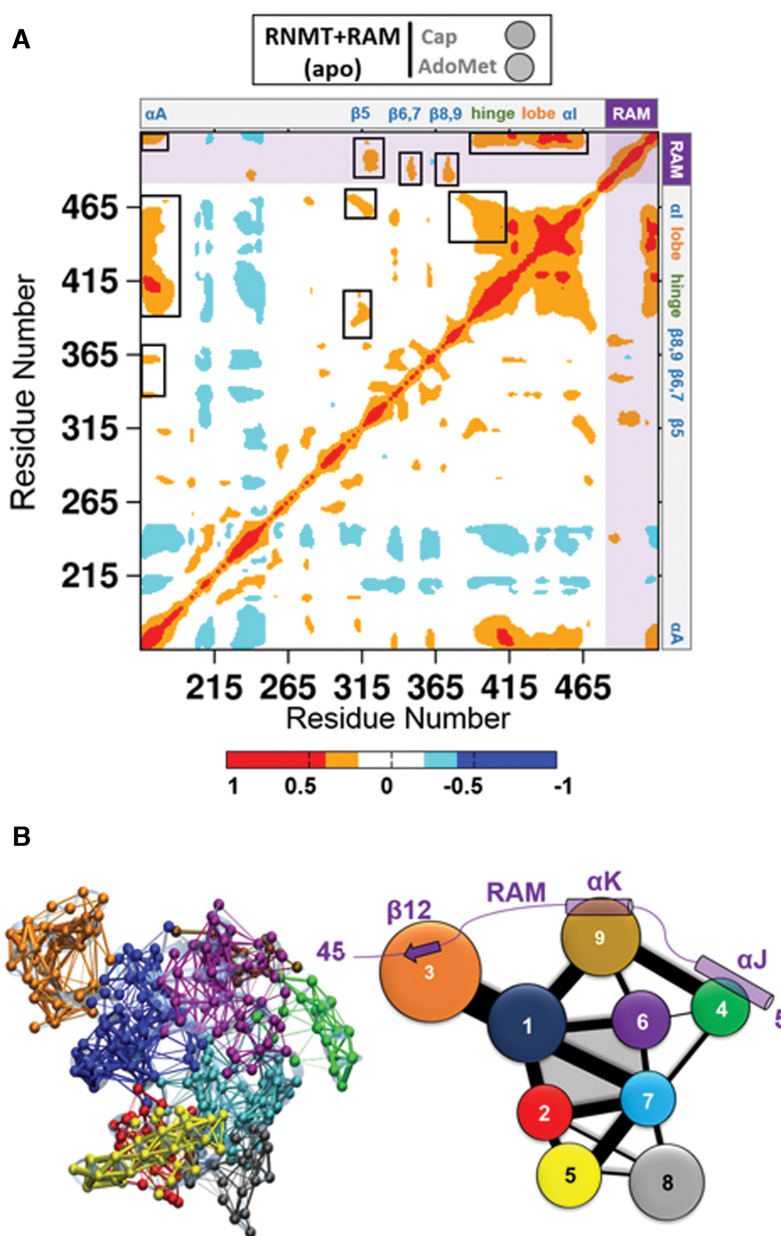
Figure 7. Allosteric networks in the RNMT–RAM complex. (**A**) Inter-residue cross-correlation plot calculated for the apo-RNMT-RAM complex. Correlations range from −1 (anti-correlated, blue) to +1 (correlated, red). Positions of the key structural elements of RNMT are indicated at the top and right. RAM is included after the RNMT C-terminus and is highlighted by shading. Strong cross-correlations that affect the RNMT active site are highlighted in black boxes in the upper triangle. (**B**) All-residue dynamic network and coarse-grained community analysis of the RNMT–RAM complex. Left: The all-residue dynamic network representation with points ('nodes') representing protein residues. The nodes are connected by the 'edges' if they are found to be within 4.5 Å of each other for at least 75% of the aMD trajectory. In addition, the nodes are coloured according to the communities they belong to. Right: 2D community diagram of RNMT–RAM. Each community is shown as a coloured circle, with a radius proportional to the size of the community (i.e. number of residues). The communities that were found to interact with each other are connected by edges, with the width of an edge proportional to intercommunity interaction strength. The active site is formed by the communities 1, 2, 6 and 7 and is shaded in grey.

in the network analysis of the complex. The community assignment is in good agreement with the structure-based domain identification in RNMT. Four communities comprise the cap and AdoMet-binding pockets: communities 1 and 2 include the upper and lower halves of helix αA, respectively; community 6 contains the β6–β9 lid region and helix αE, whereas community 7 includes the AdoMet binding Motifs I and II. These four communities displayed strong in-

tercommunity connections, which is indicated by the width of the edges in the 2D community network diagram (Figure 7B). In addition, on the periphery, community 1 partially includes the lobe region and confirms the strong connections between helix αA and the lobe.

The network analysis also provided an evidence of the allosteric communication between the RNMT active site and RAM. First, community 1 (helix αA + lobe) showed strong

connections with the C-terminal end of RAM (strand β12), which is included in community 3; second, the middle region of RAM (RAM helix αK, community 9) communicates with the active site communities 1 and 6; finally, helix J in the N-terminal region of RAM (RAM residues 2–15, community 4) showed connections with RAM helix K and also with communities 6 and 7 within the RNMT active site. The correlation and network analyses unveiled underlying long-range allosteric networks and paths that are crucial for allosteric regulation of RNMT by RAM.

RAM residues 1–20 are critical for RNMT activation

The network analysis of the *apo*-RNMT–RAM complex revealed three key regions within RAM that communicate with the RNMT active site and are important for allosteric regulation (Figure 7B), namely a short strand β12 (in the RAM C-terminus; part of community 3) and helices αK (residues 24–30; part of community 9) and αJ (in the N-terminal end; part of community 4). The first two were known to provide a key stabilization effect on the lobe and the active site residues, as was shown in our recent computational and biochemical study (8), where we described in great detail the interactions of these regions with the RNMT lobe and α helix A, as well as explored an extensive set of *in silico* and *in vitro* mutants designed to test these interactions. On the other hand, the finding that a more remote N-terminal region of RAM (residues 1–20, containing helix αJ) also participates in the allosteric networks and contributes to regulating the RNMT activity was somewhat surprising and not immediately evident from the crystal structure. It was previously shown (63) that smaller fractions of the RNMT activation domain of RAM, e.g. RAM 1–35 and RAM 20–45, are sufficient to interact with and partially stabilize RNMT; however, the entire domain (RAM 1–45) is required for maximal RNMT activation.

A careful inspection of the cMD and aMD trajectories of the *apo*-RNMT–RAM complex enabled identification of an extended contact region between the N-terminal (residues 2–18, including helix αJ) and central (residues 20–30, including helix αK) sections of RAM and the 315–375 region of RNMT (which includes helix αE, strand β9 and a long loop). Four hydrogen-bonding interactions were seen to maintain this contact and remained stable throughout entire trajectories, namely: (RAM)R18–(RNMT)Y351, (RAM)D23–(RNMT)Y274, (RAM)Y29–(RNMT)E323 and (RAM)Y29–(RNMT)N320 (Supplementary Table S3). These interactions led to significant stabilization of the β-lid positioned adjacent to the cap binding site, thus contributing to the RNMT stabilization by RAM. Since the main focus in our previous work (8) was placed on the interactions between (the C-terminal region of) RAM and the RNMT lobe, hinge and helix αJ elements, other regions were not studied in such depth. The RAM or RNMT residues participating in this novel interaction site were not investigated previously. Now, we suggest testing their importance by further mutagenesis studies. Taking into account an extended nature of this contact and presence of multiple H-bonding interactions, we note that even a removal of a single H-bond likely will not break this interface. Therefore, a more appropriate way would be a deletion

of the entire N-terminal region of RAM. This would also be consistent with the above-mentioned experiments that explored different sections of RAM (63).

To provide further support to this finding and to rationalize the experimental results (63), we designed an additional system in which the N-terminus of RAM was deleted, and simulated RNMT in complex with such a 'truncated' form of RAM (residues 20–45). The conformational behaviour of RNMT in the cMD and aMD simulations was then analysed following the above described protocols. The simulations demonstrated that the truncated RAM maintained an overall stability, with the exception of the helix αK that exhibited much higher flexibility in the absence of the RAM N-terminus, which previously acted as an additional stabilizing anchor. In turn, RNMT largely demonstrated the same structure and dynamics as in the complex with a longer RAM (Figure 8A; compare with Figure 4B). As expected, the RNMT interactions with the C-terminal region of RAM were largely unaffected by the removal of the RAM N-terminus: the RNMT lobe was still well structured in the presence of the truncated RAM and contributed to maintaining the secondary structure elements of the hinge and α-helix A. However, a notable difference was observed for the RNMT β-lid: strands β8 and β9 were significantly destabilized, inducing a conformational change within the AdoMet binding pocket.

This dynamic behaviour was rationalized by performing the network analysis in the RNMT–RAM (20–45) system. The obtained community diagram (Figure 8B) is largely identical to the one with a full-length RAM (Figure 7B), with one important exception that the removal of the RAM helix J has led to the disappearance of community 4, which previously was interacting with communities 6 and 7 that comprise the AdoMet binding site. As a result, one component of the allosteric network between RAM and RNMT has been lost and the connectivity between RAM and the AdoMet binding site was significantly reduced.

This result is fully consistent with the free-energy landscape analysis performed for the simulation with the truncated RAM. The computed FEL of the active site of RNMT has yielded a qualitatively different picture (compare Figure 8C with Figure 5D): now there is only one free energy minimum, which corresponds to the 'cap-open' state and has the same position and shape as in the case of the full-length RAM. This conformation of the active site (Figure 8C) favours binding of the cap; this is also confirmed by monitoring the volume of the cap pocket (Figure 8D), which remained largely the same as for RNMT with the full-length RAM (Figure 6C). In contrast, the previously observed second minimum, corresponding to the 'fully open' state in Figure 5D, has now completely disappeared, meaning that this conformation was not sampled at all when the N-terminal region of RAM was removed. The pocket volume analysis consistently showed that the AdoMet binding pocket has shrunk and cannot accommodate the substrate (Figure 8D). The representative snapshots provide a molecular explanation of such qualitatively different behaviour: the AdoMet binding pocket was occluded by the displacement of the strands β8-β9 and Motif I residues (Figure 8C); in particular, the sidechains of both K208 and Y289 have flipped to partially occupy the AdoMet binding site.
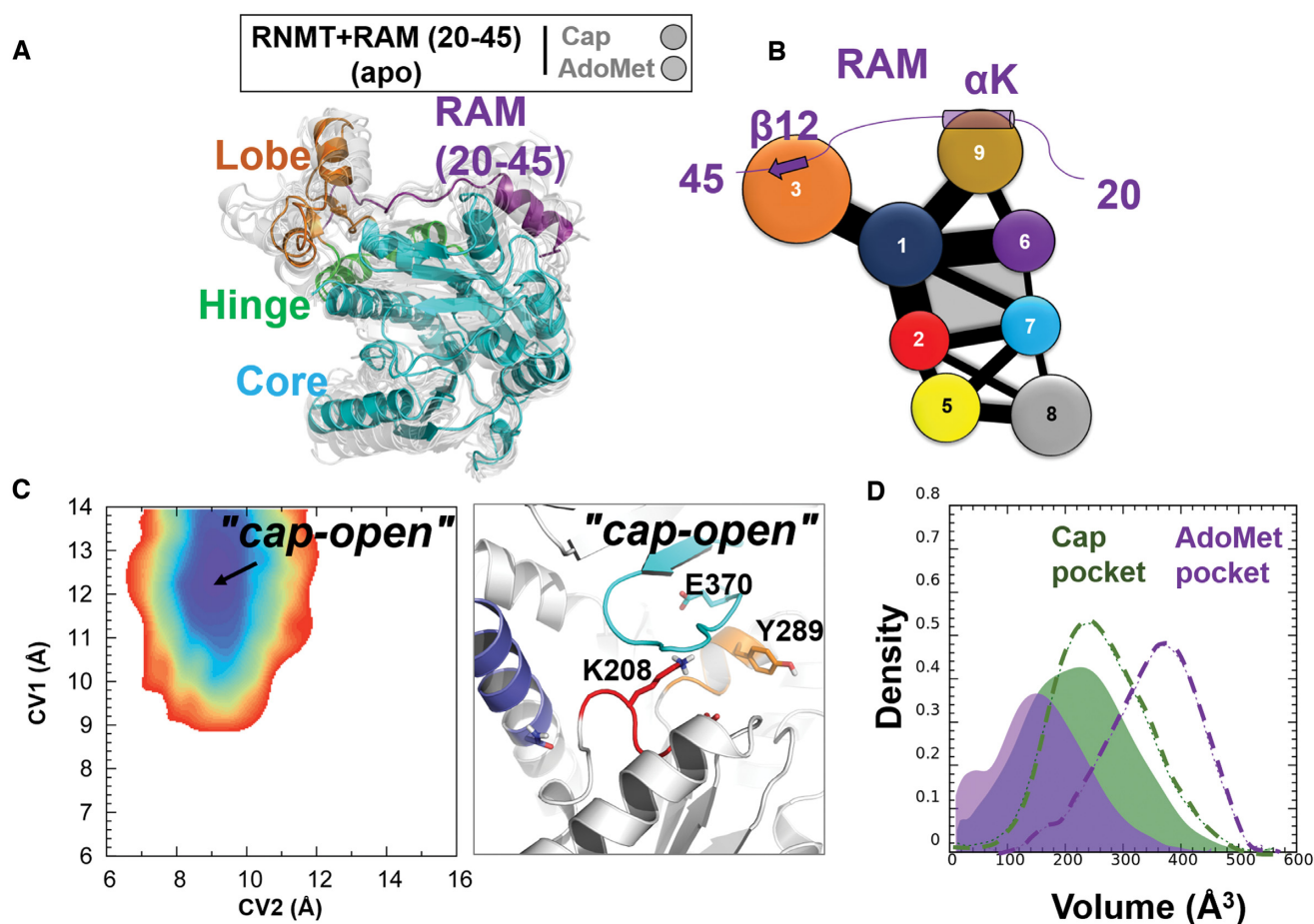
Figure 8. Modulation of the RNMT active site upon binding of a truncated form of RAM (20–45). (**A**) Conformational dynamics of RNMT in complex with the truncated RAM (20–45). The representative simulation snapshot is superimposed with multiple structures (light grey) that were sampled from the entire aMD trajectory and illustrate the range of conformational dynamics. The key structural elements are labelled and coloured as in Figure 4B. (**B**) The community network diagram of the RNMT–RAM (2–45) complex. The representation is the same as in Figure 7B. (**C**) Left: Free energy landscape (FEL) of *apo*-RNMT in complex with the truncated RAM. Right: The representative structure of the RNMT active site corresponding to the 'cap-open' state. The representation is the same as in Figure 5. (**D**) Distribution of the volume of the cap (green) and AdoMet (magenta) binding pockets during the aMD simulation of *apo*-RNMT in complex with the truncated RAM. The representation is the same as in Figure 6.

Altogether, our results provide an evidence of the importance of the RAM N-terminal region for the allosteric regulation of RNMT, and specifically its crucial role in controlling the AdoMet pocket through the allosteric network connecting the RAM N-terminus to the AdoMet binding site. The truncated RAM can still efficiently promote binding of the cap. However, in the absence of the N-terminal section of RAM, the AdoMet binding is precluded, which will affect the RNMT activity. This is consistent with the previous experimental observation (63) that a longer RAM 1–45 is required for maximal RNMT activation.

DISCUSSION

In eukaryotes, nascent RNA polymerase II transcripts are cotranscriptionally modified at the 5′ end by the addition of the mRNA cap structure that is essential for stability and efficient processing, transport and translation of the mRNA (64–66). N7-methylation of cap guanosine is catalysed by the mammalian mRNA cap methyltransferase (RNMT), which is known to be activated by RAM (7,64).

Important efforts were carried out in an attempt to shed light into the molecular basis that could explain the allosteric modulation of RNMT activity induced by RAM including biophysical, crystallographic and modelling studies (8,63,67). Molecular dynamics has grown into a robust tool for describing dynamics of biomolecular systems at atomic resolution. However, allosteric regulation involves conformational changes often taking place on the microsecond to millisecond timescales that are difficult to reach using standard molecular dynamics simulations (42,60,68,69). In this work, we investigated RNMT activation by RAM by means of accelerated molecular dynamics (aMD) simulations, a popular enhanced sampling method. aMD simulations were able to sufficiently sample the free energy landscape of RNMT and to capture the conformational changes occurring within the RNMT active site that can account for the RAM-dependent activity of the enzyme.

To date, the lack of crystallographic data of mRNA methyltransferases with simultaneously bound substrates, AdoMet and cap, challenges the clarification of this methyl-transfer mechanism. Here, we have built a model of the hu-

man RNMT–RAM complex with the bound reaction substrates and validated it by using standard MD and aMD simulations. The cap fits into a pocket formed in-between α-helix A and strands β6-β9, which form the 'lid' of the pocket, establishing polar and hydrophobic interactions with G_0 of the cap. The polyphosphate chain is stabilized by a network of highly conserved, positively charged residues, namely R173, K180 and K208, elucidating the location of the nascent mRNA transcript bound to RNMT. The methyl donor AdoMet interacts with the conserved Motif I and Motif II loops; its adenine base is stacked between I228 and the cap-stabilizing residue Y289. The binding poses of the reaction substrates bound to RNMT–RAM were maintained throughout the unrestrained aMD trajectories, and the secondary structure conformations of key structural elements of RNMT (hinge and lobe) were essentially preserved. Interestingly, when AdoMet and the cap were simulated bound to RNMT in the absence of RAM, the original binding poses were equally retained despite the remarkable flexibility of the hinge, the lobe and α-helix A. Although we cannot reject the possibility that the substrates could eventually be destabilized on a longer timescale, the results suggest that any stabilization effect of RAM on the RNMT active site mainly occurs prior to binding of the substrates.

We have explored possible mechanisms of such stabilization effect by building a comprehensive set of simulation systems (with/without substrates, with/without RAM) and performing standard and aMD simulations for them. The aMD simulations of *apo*-RNMT in the presence and absence of RAM have offered molecular and energetic insights into the RAM-induced conformational changes occurring in the RNMT active site. Free energy landscapes (FELs) representing the conformational space of the RNMT active site were computed for each simulated system. In the absence of RAM, the results suggest an equilibrium between a fully 'closed' form of *apo*-RNMT (both substrate pockets are inaccessible) and a conformation in which binding of the cap is favoured. The 'fully open' state, with optimal and accessible AdoMet and cap pockets, was not favoured in *apo*-RNMT. In contrast, the *apo*-RNMT–RAM complex has demonstrated an equilibrium between a 'fully open' conformation of the enzyme's active site and a conformation favouring binding of the cap, whereas the 'closed' state was not sampled. This finding was further explained as a result of the stability observed in α-helix A and the β8-β9 lid that favours cap binding, along with the reorientation of Y289 and Motif I loop towards the cap binding pocket, which increases the accessibility to AdoMet. aMD simulations of RNMT–RAM with a single cap substrate showed a notably reduced barrier between the 'fully open' and the 'cap-open' conformations, suggesting that the cap binding is likely to promote subsequent binding of AdoMet. This event was previously reported by our group (8) and can now be rationalized by a conformational shift of K208 towards the cap polyphosphate chain that favours the accessibility to AdoMet. It must be noted it remains possible that the induced fit mechanism might enable AdoMet or cap binding to RNMT in the absence of RAM, even when respective pockets deemed inaccessible. In summary, the studies showed that binding of RAM notably enhances selection of the RNMT active site conformations suitable for binding of substrates, providing a rationale to the increased RNMT catalytic activity measured in the presence of RAM. Interestingly, a similar conformational selection effect, revealed by simulation-based analyses, was recently reported for the binding of a GSK3 kinase to the C-terminal region of a cytoskeletal protein desmoplakin (70). Though unrelated to RNMT, together these examples show that it is becoming increasingly possible to capture subtle effects, such as the mechanisms of conformational selection and allostery, via MD simulations.

Finally, the community network analysis performed on the aMD simulations of the RNMT–RAM complex has provided evidence for the long-distance allosteric communications between RAM and the active site residues. The study has confirmed strong correlations between RAM, lobe, hinge and α-helix A. The characterized allosteric networks have offered new evidences on putative interactions with helices αE, αD, strands β6–9 and Motif I, suggesting that the N-terminal region of RAM (residues 1–20) can directly affect the RNMT active site conformations. This is in line with our identification of a novel interaction site between the N-terminal section of RAM and the 315–375 region of RNMT. This has been further confirmed by FEL of the complex of RNMT with a truncated RAM (residues 20–40), which has failed to sample the conformations suitable for AdoMet binding or the 'fully open' state. This result is in agreement with previous studies that showed that a truncated form of RAM (20–45) was able to bind to RNMT but failed in the activation process of the enzyme (7).

In summary, our simulation-based investigation has provided new insights into the molecular mechanisms of the RNMT allosteric regulation, and represents a powerful demonstration of the MD/aMD usefulness in studying allostery. We have shed light on the conformational changes communicated by RAM to the RNMT active site, which select the states that promote binding of the reaction substrates. We have identified a number of residues critical for binding of both substrates and RAM; some of these have not been previously tested by site-directed mutagenesis experiments. Moreover, this work provides the description of the binding poses of the cap and AdoMet simultaneously bound in the RNMT active site. Such information, along with deeper understanding of the mechanism of action of the RNMT–RAM complex, is critical for drug discovery efforts aiming to inhibit the cap methyltransferase activity—and thus gene expression and translation—in tumour cells or in parasites. Moreover, the recent crystallographic structures of methyltransferases from different flavivirus, such as Zika (71), constitute a very promising starting point for understanding the molecular details of the methyltransferase machinery in viruses, and will offer opportunities for structure-based rational design of antiviral inhibitors.

SUPPLEMENTARY DATA

Supplementary Data are available at NAR Online.

FUNDING

REFERENCES

1. Furuichi,Y. (2015) Discovery of m^{7}G-cap in eukaryotic mRNAs. *Proc. Jpn. Acad. Ser. B Phys. Biol. Sci.*, **91**, 394.
2. Ramanathan,A., Robb,G.B. and Chan,S.-H. (2016) mRNA capping: biological functions and applications. *Nucleic Acids Res.*, **44**, 7511–7526.
3. Galloway,A. and Cowling,V.H. (2018) mRNA cap regulation in mammalian cell function and fate. *Biochim. Biophys. Acta Gene Regul. Mech.*, **3**, 270–279.
4. Shuman,S. (2000) Structure, mechanism, and evolution of the mRNA capping apparatus. *Prog. Nucleic Acid Res. Mol. Biol.*, **66**, 1–40.
5. Shuman,S. (2002) What messenger RNA capping tells us about eukaryotic evolution. *Nat. Rev. Mol. Cell Biol.*, **3**, 619–625.
6. Gonatopoulos-Pournatzis,T. and Cowling,V.H. (2014) RAM function is dependent on Kapβ2-mediated nuclear entry. *Biochem. J.*, **3**, 473–484.
7. Gonatopoulos-Pournatzis,T., Dunn,S., Bounds,R. and Cowling,V.H. (2011) RAM/Fam103a1 is required for mRNA cap methylation. *Mol. Cell*, **44**, 585–596.
8. Varshney,D., Petit,A.-P., Bueren-Calabuig,J.A., Jansen,C., Fletcher,D.A., Peggie,M., Weidlich,S., Scullion,P., Pisliakov,A.V. and Cowling,V.H. (2016) Molecular basis of RNA guanine-7 methyltransferase (RNMT) activation by RAM. *Nucleic Acids Res.*, **44**, 10423–10436.
9. Grasso,L., Suska,O., Davidson,L., Gonatopoulos-Pournatzis,T., Williamson,R., Wasmus,L., Wiedlich,S., Peggie,M., Stavridis,M.P. and Cowling,V.H. (2016) mRNA Cap methylation in pluripotency and differentiation. *Cell Rep.*, **16**, 1352–1365.
10. Aregger,M. and Cowling,V.H. (2013) Human cap methyltransferase (RNMT) N-terminal non-catalytic domain mediates recruitment to transcription initiation sites. *Biochem. J.*, **455**, 67–73.
11. Glover-Cutter,K., Kim,S., Espinosa,J. and Bentley,D.L. (2008) RNA polymerase II pauses and associates with pre-mRNA processing factors at both ends of genes. *Nat. Struct. Mol. Biol.*, **15**, 71–78.
12. Aregger,M., Kaskar,A., Varshney,D., Fernandez-Sanchez,M.E., Inesta-Vaquera,F.A., Weidlich,S. and Cowling,V.H. (2016) CDK1-Cyclin B1 activates RNMT, coordinating mRNA cap methylation with G1 phase transcription. *Mol. Cell*, **61**, 734–746.
13. Fabrega,C., Hausmann,S., Shen,V., Shuman,S. and Lima,C.D. (2004) Structure and mechanism of mRNA cap (guanine-N7) methyltransferase. *Mol. Cell*, **13**, 77–89.
14. Martin,J.L. and McMillan,F.M. (2002) SAM (dependent) I AM: the S-adenosylmethionine-dependent methyltransferase fold. *Curr. Opin. Struct. Biol.*, **12**, 783–793.
15. Varshney,D., Lombardi,O., Schweikert,G., Dunn,S., Suska,O. and Cowling,V.H. (2018) mRNA cap methyltransferase, RNMT-RAM, promotes RNA Pol II-dependent transcription. *Cell Rep.*, **23**, 1530–1542.
16. Peña,la, De,M., Kyrieleis,O.J.P. and Cusack,S. (2007) Structural insights into the mechanism and evolution of the vaccinia virus mRNA cap N7 methyl-transferase. *EMBO J.*, **26**, 4913–4925.
17. Kannan,S., Venkatachalam,G., Lim,H.H., Surana,U. and Verma,C. (2018) Conformational landscape of the epidermal growth factor receptor kinase reveals a mutant specific allosteric pocket. *Chem. Sci.*, **9**, 5212–5222.
18. Palermo,G., Ricci,C.G., Fernando,A., Basak,R., Jinek,M., Rivalta,I., Batista,V.S. and McCammon,J.A. (2017) Protospacer adjacent Motif-Induced allostery activates CRISPR-Cas9. *J. Am. Chem. Soc.*, **139**, 16028–16031.
19. Mou,L., Cui,T., Liu,W., Zhang,H., Cai,Z., Lu,S. and Gao,G. (2016) Microsecond molecular dynamics simulations provide insight into the ATP-competitive inhibitor-induced allosteric protection of Akt kinase phosphorylation. *Chem. Biol. Drug Des.*, **89**, 723–731.
20. Hertig,S., Latorraca,N.R. and Dror,R.O. (2016) Revealing Atomic-Level mechanisms of protein allostery with molecular dynamics simulations. *PLoS Comput. Biol.*, **12**, e1004746.
21. Miao,Y., Feixas,F., Eun,C. and McCammon,J.A. (2015) Accelerated molecular dynamics simulations of protein folding. *J. Comput. Chem.*, **36**, 1536–1549.
22. Pang,Y.T., Miao,Y. and Wang,Y. (2016) Gaussian accelerated molecular dynamics in NAMD. *J. Chem. Theory Comput.*, **13**, 9–19.
23. Kastner,K.W. and Izaguirre,J.A. (2016) Accelerated molecular dynamics simulations of the octopamine receptor using GPUs: discovery of an alternate agonist-binding position. *Proteins*, **84**, 1480–1489.
24. Hamelberg,D., Mongan,J. and McCammon,J.A. (2004) Accelerated molecular dynamics: a promising and efficient simulation method for biomolecules. *J. Chem. Phys.*, **120**, 11919–11929.
25. Bernardi,R.C., Melo,M.C.R. and Schulten,K. (2015) Enhanced sampling techniques in molecular dynamics simulations of biological systems. *Biochim. Biophys. Acta*, **1850**, 872–877.
26. Yadahalli,S., Li,J., Lane,D.P., Gosavi,S. and Verma,C.S. (2017) Characterizing the conformational landscape of MDM2-binding p53 peptides using Molecular Dynamics simulations. *Sci. Rep.*, **7**, 15600.
27. Case,D.A., Babin,V., Berryman,J.T., Betz,R.M., Cai,Q., Cerutti,D.S., Cheatham,T.E., Darden,T.A., Duke,R.E., Gohlke,H. *et al.* (2014) *AMBER 14*. University of California, San Francisco.
28. Maier,J.A., Martinez,C. and Kasavajhala,K. (2015) ff14SB: improving the accuracy of protein side chain and backbone parameters from ff99SB. *J. Chem. Theory Comput.*, **11**, 3696–3713.
29. Frisch,M.J., Trucks,G.W., Schlegel,H.B., Scuseria,G.E., Robb,M.A., Cheeseman,J.R., Montgomery,J.A. Jr, Vreven,T., Kudin,K.N. *et al.* (2004) *Gaussian 03, Revision C.02*. Gaussian, Inc., Wallingford CT.
30. Cornwell,W.D., Cieplak,P., Bayly,C.I. and Kollman,P.A. (1993) Application of RESP charges to calculate conformational energies, hydrogen bond energies, and free energies of solvation. *J. Am. Chem. Soc.*, **115**, 9620–9631.
31. Wang,J., Wolf,R.M., Caldwell,J.W., Kollman,P.A. and Case,D.A. (2004) Development and testing of a general amber force field. *J. Comput. Chem.*, **26**, 114–114.
32. Jorgensen,W.L., Chandrasekhar,J., Madura,J.D., Impey,R.W. and Klein,M.L. (1983) Comparison of simple potential functions for simulating liquid water. *J. Chem. Phys.*, **79**, 926–935.
33. Darden,T., York,D. and Pedersen,L. (1993) Particle mesh Ewald: An N·log(N) method for Ewald sums in large systems. *J. Chem. Phys.*, **98**, 10089–10092.
34. Ryckaert,J.-P., Ciccotti,G. and Berendsen,H.J.C. (1977) Numerical integration of the cartesian equations of motion of a system with constraints: molecular dynamics of n-alkanes. *J. Comput. Phys.*, **23**, 327–341.
35. Berendsen,H.J.C., Postma,J.P.M., van Gunsteren,W.F., DiNola,A. and Haak,J.R. (1984) Molecular dynamics with coupling to an external bath. *J. Chem. Phys.*, **81**, 3684–3690.
36. Markwick,P.R.L. and McCammon,J.A. (2011) Studying functional dynamics in bio-molecules using accelerated molecular dynamics. *Phys. Chem. Chem. Phys.*, **13**, 20053–20065.
37. Hamelberg,D., de Oliveira,C.A.F. and McCammon,J.A. (2007) Sampling of slow diffusive conformational transitions with accelerated molecular dynamics. *J. Chem. Phys.*, **127**, 155102–155109.
38. Hamelberg,D., Mongan,J. and McCammon,J.A. (2004) Accelerated molecular dynamics: a promising and efficient simulation method for biomolecules. *J. Chem. Phys.*, **120**, 11919–11929.
39. Iannuzzi,M., Laio,A. and Parrinello,M. (2003) Efficient exploration of reactive potential energy surfaces using car-Parrinello molecular dynamics. *Phys. Rev. Lett.*, **90**, 238302.
40. Laio,A. and Parrinello,M. (2002) Escaping free-energy minima. *Proc. Natl. Acad. Sci. U.S.A.*, **99**, 12562–12566.
41. Caliman,A.D., Miao,Y. and McCammon,J.A. (2017) Activation mechanisms of the first sphingosine-1-phosphate receptor. *Protein Sci.*, **26**, 1150–1160.
42. Miao,Y., Goldfeld,D.A., Moo,E.V., Sexton,P.M., Christopoulos,A., McCammon,J.A. and Valant,C. (2016) Accelerated structure-based design of chemically diverse allosteric modulators of a muscarinic G protein-coupled receptor. *Proc. Natl. Acad. Sci. U.S.A.*, **113**, E5675–E5684.

43. Bueren-Calabuig,J.A. and Michel,J. (2016) Impact of Ser17 phosphorylation on the conformational dynamics of the oncoprotein MDM2. *Biochemistry*, **55**, 2500–2509

44. Bueren-Calabuig,J.A. and Michel,J. (2015) Elucidation of Ligand-Dependent modulation of Disorder-Order transitions in the oncoprotein MDM2. *PLoS Comput. Biol.*, **11**, e1004282.

45. Pierce,L.C.T., Salomon-Ferrer,R., Augusto F de Oliveira,C., McCammon,J.A. and Walker,R.C. (2012) Routine access to millisecond time scale events with accelerated molecular dynamics. *J. Chem. Theory Comput.*, **114**, 2997–3002.

46. Bucher,D., Grant,B.J., Markwick,P.R. and McCammon,J.A. (2011) Accessing a hidden conformation of the maltose binding protein using accelerated molecular dynamics. *PLoS Comput. Biol.*, **7**, e1002034.

47. Delano,W.L. (2002) *The PyMOL Molecular Graphics System*. DeLano Scientific, San Carlos.

48. Humphrey,W., Dalke,A. and Schulten,K. (1996) VMD: Visual molecular dynamics. *J. Mol. Graph.*, **14**, 33–38.

49. Hünenberger,P.H., Mark,A.E. and van Gunsteren,W.F. (1995) Fluctuation and cross-correlation analysis of protein motions observed in nanosecond molecular dynamics simulations. *J. Mol. Biol.*, **252**, 492–503.

50. Laskowski,R.A. and Swindells,M.B. (2011) LigPlot+: multiple ligand-protein interaction diagrams for drug discovery. *J. Chem. Inf. Model.*, **51**, 2778–2786.

51. Schmidtke,P., Bidon-Chanal,A., Luque,F.J. and Barril,X. (2011) MDpocket: open-source cavity detection and characterization on molecular dynamics trajectories. *Bioinformatics*, **27**, 3276–3285.

52. Baker,N.A., Sept,D., Joseph,S., Holst,M.J. and McCammon,J.A. (2001) Electrostatics of nanosystems: application to microtubules and the ribosome. *Proc. Natl. Acad. Sci. U.S.A.*, **98**, 10037–10041.

53. Wang,Y. and McCammon,J.A. (2012) Accelerated molecular dynamics: Theory, implementation and applications. *AIP Conf. Proc.*, **1456**, 165–172.

54. Shen,T. and Hamelberg,D. (2008) A statistical analysis of the precision of reweighting-based simulations. *J. Chem. Phys.*, **129**, 034103.

55. Miao,Y., Nichols,S.E. and McCammon,J.A. (2014) Free energy landscape of G-protein coupled receptors, explored by accelerated molecular dynamics. *Phys. Chem. Chem. Phys.*, **14**, 6398–63406.

56. Zhao,B., Stuart,M.A.C. and Hall,C.K. (2017) Navigating in foldonia: Using accelerated molecular dynamics to explore stability, unfolding and self-healing of the β-solenoid structure formed by a silk-like polypeptide. *PLoS Comput. Biol.*, **13**, e1005446.

57. Eargle,J. and Luthey-Schulten,Z. (2012) NetworkView: 3D display and analysis of protein·RNA interaction networks. *Bioinformatics*, **28**, 3000–3001.

58. Sethi,A., Eargle,J., Black,A.A. and Luthey-Schulten,Z. (2009) Dynamical networks in tRNA:protein complexes. *Proc. Natl. Acad. Sci. U.S.A.*, **106**, 6620–6625.

59. Girvan,M. and Newman,M. (2002) Community structure in social and biological networks. *Proc. Natl. Acad. Sci. U.S.A.*, **99**, 7821–7826.

60. Gasper,P.M., Fuglestad,B., Komives,E.A., Markwick,P.R.L. and McCammon,J.A. (2012) Allosteric networks in thrombin distinguish procoagulant vs. anticoagulant activities. *Proc. Natl. Acad. Sci. U.S.A.*, **109**, 21216–21222.

61. Bora,R.P., Chu,Z.T. and Warshel,A. (2015) Methyltransferases do not work by compression, cratic, or desolvation effects, but by electrostatic preorganization. *Proteins*, **83**, 318–330

62. VanWart,A.T., Eargle,J., Luthey-Schulten,Z. and Amaro,R.E. (2012) Exploring residue component contributions to dynamical network models of allostery. *J. Chem. Theory Comput.*, **8**, 2949–2961

63. Gonatopoulos,T. (2014) RAM function is dependent on Kapβ2-mediated nuclear entry. *Biochemic.*, **457**, 473–484

64. Cowling,V.H. (2009) Regulation of mRNA cap methylation. *Biochem. J.*, **425**, 295–302.

65. Moore,M.J. and Proudfoot,N.J. (2009) Pre-mRNA processing reaches back to transcription and ahead to translation. *Cell*, **136**, 688–700.

66. Cougot,N., van Dijk,E., Babajko,S. and Séraphin,B. (2004) 'Cap-tabolism'. *Trends Biochem. Sci.*, **29**, 436–444.

67. Gonatopoulos-Pournatzis,T., Dunn,S. and Bounds,R. (2011) RAM/Fam103a1 is required for mRNA cap methylation. *Mol. Cell*, **44**, 585–596.

68. Oyen,D., Fenwick,R.B., Stanfield,R.L., Dyson,H.J. and Wright,P.E. (2015) Cofactor-mediated conformational dynamics promote product release from Escherichia coli dihydrofolate reductase via an Allosteric Pathway. *J. Am. Chem. Soc.*, **137**, 9459–9468.

69. Lipchock,J.M. and Loria,J.P. (2010) Nanometer propagation of millisecond motions in V-type allostery. *Structure*, **18**, 1596–1607.

70. McAnany,C.E. and Mura,C. (2016) Claws, disorder, and conformational dynamics of the C terminal region of human desmoplakin. *J. Phys. Chem. B*, **120**, 8654–8667.

71. Duan,W., Song,H., Wang,H., Chai,Y., Su,C., Qi,J., Shi,Y. and Gao,G.F. (2017) The crystal structure of Zika virus NS5 reveals conserved drug targets. *EMBO J.*, **36**, 919–933.